# Mechanical properties of compacted graphite cast iron with different microstructures

**R. W. Gregorutti* and J. E. Grau**

Tensile strength, fracture toughness and impact properties were evaluated in compacted graphite (CG) cast iron with ferritic, pearlitic and ausferritic microstructures. Ultimate tensile strengths for the ferritic and pearlitic samples were 337 and 632 MPa respectively. The austempered samples showed a significant increment in the strength and recording values between 675 and 943 MPa. The fracture toughness test revealed that the stress–intensity factor $K_{IC}$ was 34·0 MPa $m^{1/2}$ for the ferritic CG iron, 39·7 MPa $m^{1/2}$ for the pearlitic and between 51·0 and 58·0 MPa $m^{1/2}$ for the austempered irons. On the other hand, CG iron with ferritic matrix exhibited the best impact properties with absorbed energy of 33·3 J. The absorbed energy of the pearlitic CG iron was the lowest, 14·3 J, while the austempered samples showed values between 17·2 and 28·4 J. Complementing these results, the critical crack size was also analysed.

**Keywords:** Compacted graphite cast iron, Microstructures, Mechanical properties

## Introduction

Compacted graphite (CG) cast iron is part of the cast iron family belonging to the Fe–C irregular eutectic system, characterised by an intermediate graphite morphology between the classical flake and nodular graphite irons (FG and NG respectively). Many studies have been performed to elucidate the features of the solidification and the graphite morphological modification in these materials,[1–9] since the physical, chemical and mechanical properties depend on the graphite morphology, in addition to the microstructure of the matrix. In CG iron, the graphite is interconnected as in the case of the FG iron but exhibiting a compact shape, with rounded tips. Studies performed to determine the compactness of the graphite particles revealed that the ratio between the length $L$ and the width $d$ ($L/d$) is in the range of 2–10 in CG, while for FG, $L/d$ is $>30$.[4] These morphological characteristics confer to CG an acceptable mechanical resistance, plasticity and high thermal conductivity. The convergence of these features promotes a higher thermal fatigue resistance,[10,11] property that allows the use of CG iron in components subjected to thermal shocks. The industrial applications of CG began in the 1960s with the manufacturing of components for heavy vehicles as truck, tractors, passenger cars and cylinder heads for large marine diesel engines.[12] In the last years, the interest in this material has been increasing, particularly in the automotive industry for the production of cylinder blocks for high performance diesel engines, since its better mechanical properties compared with FG iron allow a considerable reduction in the weight of this component. At the same time, it was reported the use of CG iron in railway brake discs in order to improve the braking performance and lifetime.[13–17]

As in the case of austempered ductile iron (ADI), the mechanical properties of CG irons can be improved by means of the austempering heat treatment, which could extend the use of this material to diverse industrial applications. The austempered microstructure is composed of acicular ferrite and high carbon austenite, commonly called ausferrite, and the kinetics of the transformation was studied in previous articles by means of the Johnson–Mehl–Avrami formalism.[18–20]

Considering that CG iron is suitable for manufacturing components, which are prone to cracking by thermal fatigue, the present work analyses the tensile strength, fracture toughness and impact properties of this material with ferritic, pearlitic and ausferritic microstructures, obtained by the corresponding heat treatments.

## Experimental

Base metal of composition 3·60C–1·80Si–0·10Mn–0·05Cu–0·027P–0·01S–0·040Cr–0·030Ni (in wt-%) was used to produce CG iron in a medium frequency induction furnace using the sandwich technique in ladle. Compacted graphite morphology was obtained by adding 0·4%FeSiMgCeCa alloy (8–10 Mg, 44–47 Si, 0·7–1·5 Ca, 1–1·2 Ce, balance Fe, in wt-%) to the liquid metal at 1450°C.

Electrolytic Cu, FeMn (60 wt-%Mn) and FeSi (75 wt-%Si) were added for Cu, Mn and Si balances respectively. The resulting chemical composition in wt-% was as follows: Fe–3·38C–2·56Si–0·48Mn–0·52Cu–0·014S–0·020P–0·035Cr–0·027Ni. Samples for mechanical testing were obtained from 25·4 mm 'Y' blocks (ASTM A-395) cast in sand moulds. Ferritic microstructure was

Laboratorio de Entrenamiento Multidisciplinario para la Investigación Tecnológica (LEMIT-CICPBA), Av. 52 s/n e/121 y 122, La Plata, B1900AYB, Argentina

*Corresponding author, email metalurgia@lemit.gov.ar


Received 7 June 2013; accepted 25 April 2014
DOI 10.1179/1743133614Y.0000000118

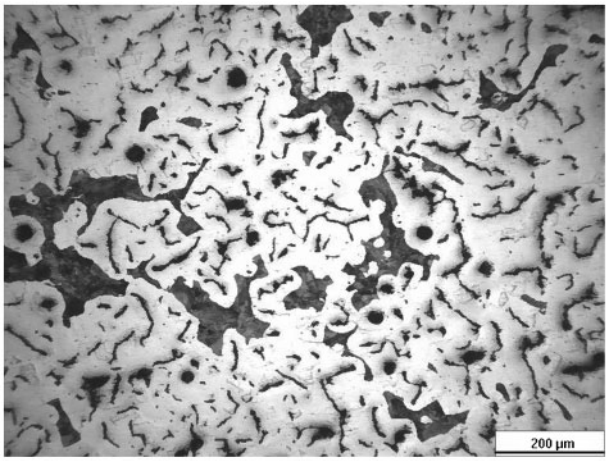


**1 As cast microstructure obtained in sand mould**

obtained by annealing, heating up to 900°C and cooling in furnace, while for the pearlitic matrix, the cooling was performed in air. Ausferritic microstructures were obtained by austempering heat treatment, austenitising at 900°C for 1 h and posterior, quenching in salt bath held at 300, 350 and 400°C, in that order, during 60 min. Optical and scanning electron microscopes were used for metallographic analysis. As cast microstructure was characterised by means of a Buehler quantitative image analyser with Omnimet Enterprise software. The retained austenite in the austempered samples was measured by X-ray diffraction using Philips PW3710 diffractometer with Cu $K_\alpha$ radiation. Single edge notched bend sample (ASTM E399-90 Standard) was used for the fracture toughness test. Mechanical properties were evaluated through tensile tests on samples of 6·25 mm diameter (ASTM E8-98 Standard) using an Instron machine of 15 ton capacity. Charpy impact test was performed on unnotched samples (ASTM A327M-91 Standard) using an AMSLER pendulum impact test machine with capacity of 300 J. Hardness measurements were performed by Brinell procedure using 2·5 mm diameter steel ball and load of 187·5 kg.

## Results and discussion

### Microstructural analysis

Figure 1 shows the as cast microstructure mostly composed by ferrite and small quantities of pearlite. The results obtained from the quantitative image analyser made in 10 different fields revealed a ratio of ~80% ferrite and ~20% pearlite.

As cast microstructure depends on the carbon equivalent, the alloying elements and the cooling rate. The carbon equivalent of the analysed CG iron was 4·24, close to the eutectic composition of 4·3. Thus, the greater amount of ferrite obeys the low amount of pearlite stabilising alloying elements as Mn and Cu, and the low cooling rate produced by the sand mould.

At the same time as the ferrite/pearlite ratio, it was determined the amount of graphite particles per square millimetre (p $mm^{-2}$) and the compacted graphite percentage. Measurements were made in 10 different fields, and the average result was 110 p $mm^{-2}$, from which the percentage of compacted graphite was in the range of 85–95% and the nodular graphite between 5 and 15%.

Ferritic and pearlitic microstructures, obtained by ferritising annealing and normalising heat treatments respectively, are shown in Fig. 2.

The thermal cycling of these heat treatments differs in the cooling rate after the austenitising step. In the ferritising annealing, the cooling is performed in furnace because it should be slow enough to allow the diffusion of carbon from the austenite to graphite particles. In this condition, the austenite remains a carbon concentration close to the equilibrium and will transform to ferrite following the stable Fe–C phase diagram. Conversely, the cooling rate in the normalising heat treatment is higher because it is carried out in air. This fact reduces significantly the carbon diffusion rate, whereby the carbon atoms will not have enough time to diffuse to the graphite particles. For this reason, the carbon content of the austenite is greater than the equilibrium concentration, leading to the eutectoid transformation austenite–pearlite.

The high cooling rate in normalising also promotes the formation of a fine pearlite, as shown in Fig. 2*b*, where it can be also observed a ferritic halo around the compacted graphite, as occurs in NG iron, denoting that the transformation was not complete.

Ausferritic microstructures obtained by the austempering heat treatments are illustrated in Fig. 3.

The ausferritic microstructure is composed by ferrite and high carbon austenite. The austempering transformation begins with the nucleation of ferrite needles, which,

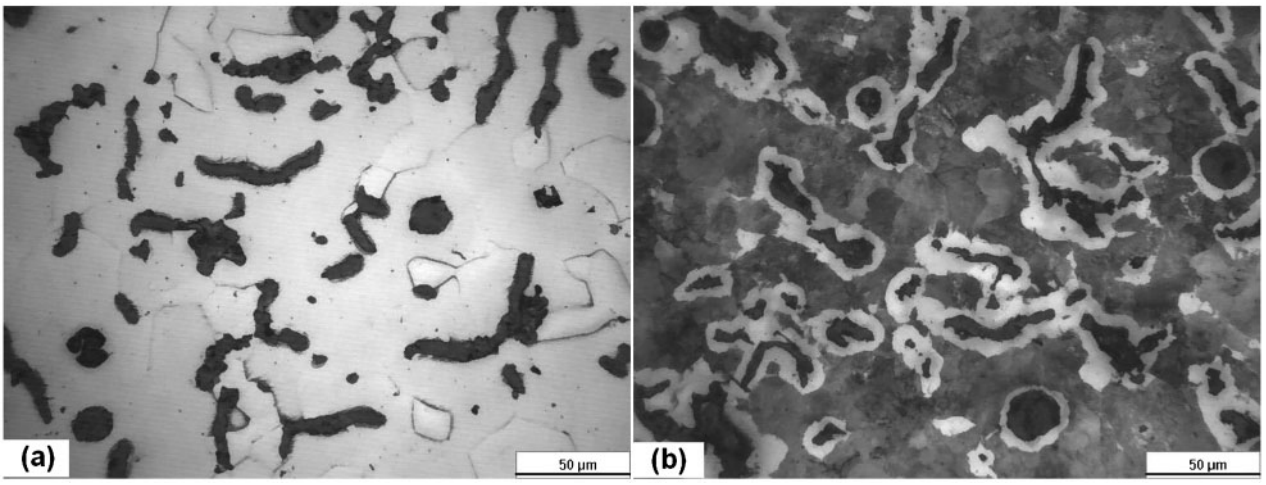


**2 *a* ferritic and *b* pearlitic microstructures obtained by heat treatment**

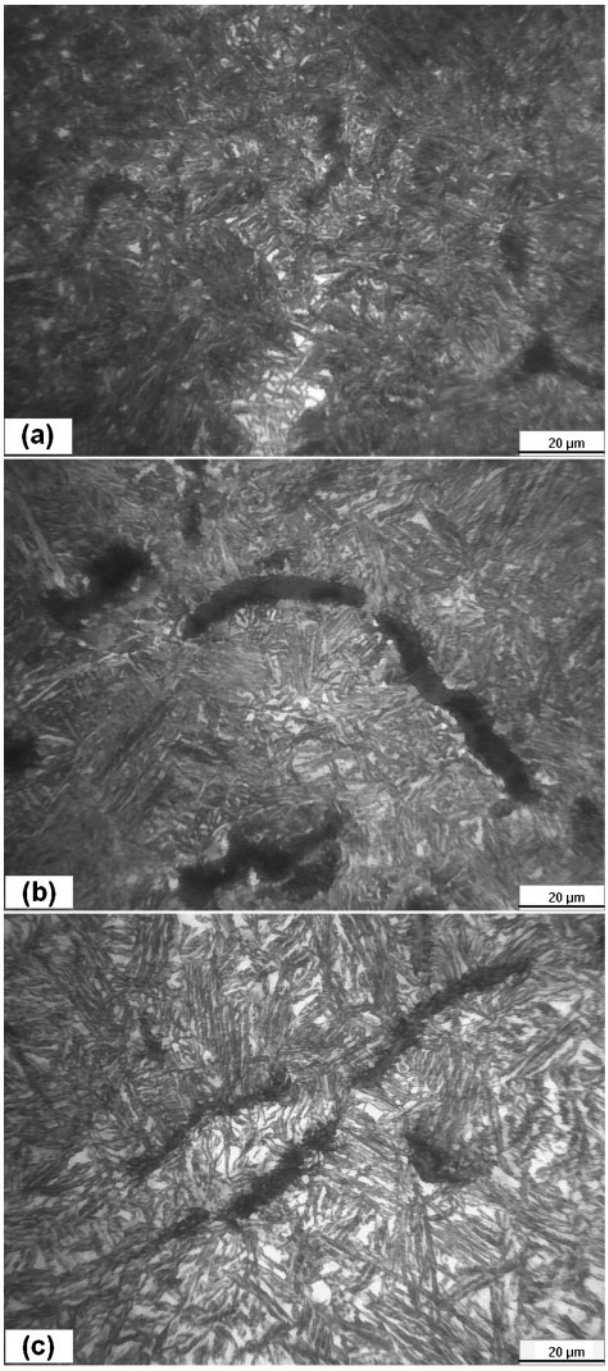


*a* at 300°C; *b* at 350°C; *c* at 400°C

**3 Austempered microstructures**

during growth, reject carbon atoms into the surrounding austenite, stabilising this phase. The driving force for the transformation is the undercooling generated between the austenitising and the austempering temperatures ($T_\gamma$ and $T_a$ respectively). At a given $T_\gamma$, the relation between ferrite and high carbon austenite varies with $T_a$, as indicated in the scheme of Fig. 4 reported by Bayati *et al.*,[21] in which the $\alpha+\gamma$ field is extended to the range of austempering temperatures.

Applying the lever rule at $T_{a1}$, the amount of retained austenite is defined by the relationship $\overline{AB}/\overline{AC}$, while at a higher $T_{a2}$, the ratio is $\overline{A'B'}/\overline{A'C'}$. As $\overline{A'B'}$ is greater than $\overline{AB}$ and $\overline{A'C'}$ is lower than $\overline{AC}$, it follows that the percentage of retained austenite increases with Ta, and consequently, the amount of ferrite will be lower.

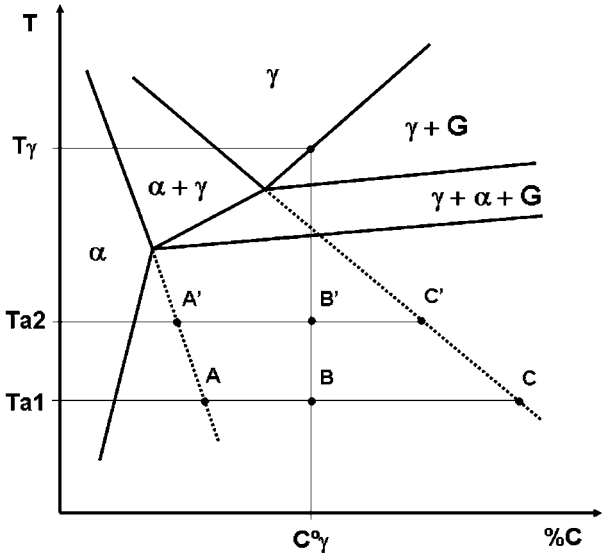


**4 Schematic illustration of phase relationship as function of $T_a$**

At a lower $T_a$, the nucleation rate of ferrite needles is greater because of the higher undercooling from $T_\gamma$, and consequently, their growth is inhibited. This feature leads to a finer and more acicular microstructure with smaller areas of austenite, as illustrated in Fig. 3*a*, corresponding to the sample austempered at 300°C. In contrast, the increment of $T_a$ reduces the nucleation rate of ferrite needles as a consequence of the lower undercooling promoted. In such situation, the fewer ferrite needles are able to grow enclosing large areas of austenite, forming a vast microstructure, as in the case of the sample austempered at 400°C shown in Fig. 3*c*.

The variation of the retained austenite with the austempering temperature was measured by X-ray diffraction, being the results recorded in Table 1.

## Analysis of mechanical properties

Table 2 reports the values of the tensile and hardness tests for the different CG irons. It is well known that the mechanical properties of CG iron increase with the content of nodules. For this reason, the percentage of compact graphite corresponding to each sample was also included.

Ultimate tensile strength (UTS), yield strength (YS) and hardness for the ferritic and pearlitic CG iron are in agreement with data reported by Stefanescu *et al.*[22] The high values of UTS, YS and particularly hardness of the pearlitic CG iron can be attributed to the small pearlite spacing, consequence of the fast cooling rate during normalising treatment.

Ausferritic microstructures reported a significant increase in the mechanical properties, noting that UTS, YS and hardness increase as the austempering temperature decreases. This behaviour is because the

**Table 1 Volume fraction of retained austenite**

| Austempering temperature/°C | Austenite/% |
|---|---|
| 300 | 28 |
| 350 | 35 |
| 400 | 39 |

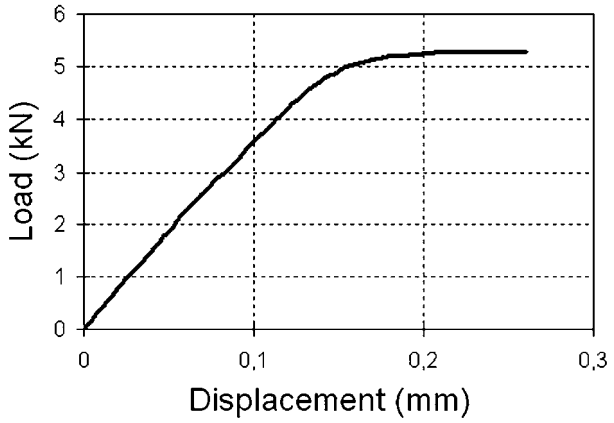


**5 Load–displacement curve of CG iron**

microstructure becomes finer and more acicular at lower Ta, as shown in Fig. 3.

On the other hand, the Young's modulus $E$, which indicates the capacity for elastic deformation of materials, recorded random values with respect to the different matrices, being in the range between 114 and 133 GPa. These results could be ascribed to the arbitrary distribution and the morphological characteristics of the graphite particles, which are embedded in the metallic matrix forming a network. This graphite network generates a significant discontinuity in the matrix, affecting the capacity for elastic deformation.

Compacted graphite iron with ferritic matrix showed the greatest ductility, with elongation of 4·4%, while for the pearlitic matrix, the elongation decreases significantly down to 1·0%. In the case of the austempered matrices, the ductility was directly related to the content of retained austenite. The microstructure obtained at 300°C recorded the lowest value of elongation, 0·8%, as a consequence of the lower amount of retained austenite displayed in Table 1, while at 350 and 400°C, the elongation increases up to 1·1 and 2·8% respectively.

It is noticeable that the sample austempered at 400°C and the pearlitic recorded close values of UTS and YS. Nevertheless, the elongation of the ausferritic sample was significantly higher, since the presence of austenite in the microstructure confers greater ductility.

## Fracture toughness test

Fracture toughness measures the resistance to extension of a crack. This property was evaluated by means of the linear elastic fracture mechanics, which define the stress–intensity factor $K_{IC}$. This parameter represents the inherent ability of a material to resist progressive tensile crack extension. The greater the value of $K_{IC}$, the higher the stress required to produce rapid propagation and the greater the resistance of the material to brittle fracture.[23]

The factor $K_{IC}$ was calculated using the following relationship, given by ASTM E399 Standard

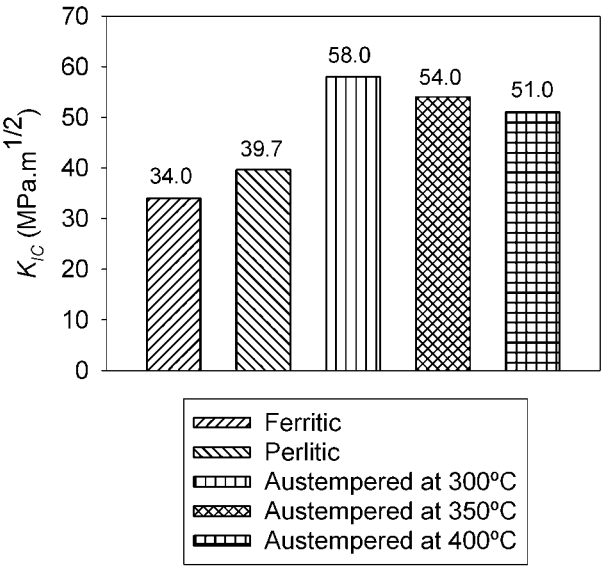


**6 Stress–intensity factor $K_{IC}$ obtained for different matrices**

$$K_{IC} = \frac{P_Q S}{B W^{3/2}} \times f\left(\frac{a}{W}\right) \quad (1)$$

Being

$$f\left(\frac{a}{W}\right) = 2{\cdot}9\left(\frac{a}{W}\right)^{1/2} + 4{\cdot}6\left(\frac{a}{W}\right)^{3/2} + 21{\cdot}8\left(\frac{a}{W}\right)^{5/2} + 37{\cdot}6\left(\frac{a}{W}\right)^{7/2} + 38{\cdot}7\left(\frac{a}{W}\right)^{9/2} \quad (2)$$

where $a$ is the length of the notch, $B$ and $W$ are the height and thickness of the single edge notched bend sample respectively, and $S$ is the distance between the support roll centres, $S=4W$.

Figure 5 illustrates the load–displacement curve obtained for CG iron that shows the evolution of the crack extension because of the action of the applied load.

The load–displacement curve exhibits a non-linear behaviour, reason by which $K_{IC}$ was calculated using the maximum load criterion, assuming that $P_Q=P_{max}$, as reported in previous works performed in FG iron.[24,25]

The results represented in Fig. 6 indicated that ferritic CG iron reported the lowest value of fracture toughness, its $K_{IC}$ being 34·0 MPa m$^{1/2}$. This property was improved with the normalising treatment, since $K_{IC}$ for the pearlitic iron was 39·7 MPa m$^{1/2}$, although the higher values were obtained by means of the austempering heat treatment. The CG iron austempered at 300°C exhibited the highest value of $K_{IC}$, 58·0 MPa m$^{1/2}$, while the values of samples austempered at 350 and 400°C were 54·0 and 51·0 MPa m$^{1/2}$ respectively.

**Table 2 Mechanical properties obtained for different matrices**

| CG iron matrix | UTS/MPa | YS/MPa | *E*/GPa | δ/% | HB | CG/% |
|---|---|---|---|---|---|---|
| Ferritic | 337 | 243 | 123 | 4·4 | 153 | 95 |
| Pearlitic | 632 | 411 | 114 | 1·0 | 257 | 90 |
| Austempered at 300°C | 943 | 700 | 132 | 0·8 | 410 | 85 |
| Austempered at 350°C | 848 | 546 | 117 | 1·1 | 354 | 90 |
| Austempered at 400°C | 675 | 450 | 133 | 2·8 | 292 | 95 |

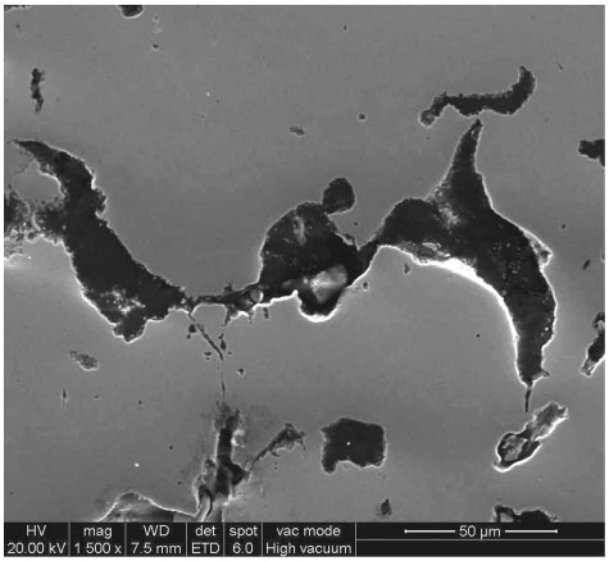


**7 Crack progress through graphite/matrix interface**

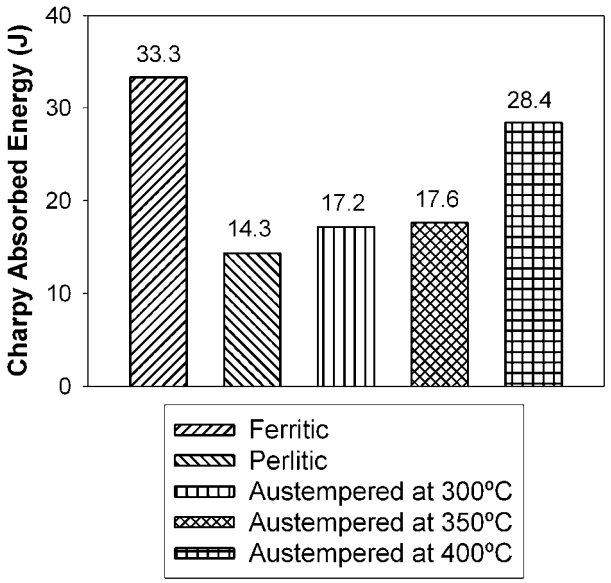


**8 Charpy absorbed energy obtained for different matrices**

The results of the fracture toughness tests have shown a similar tendency to the mechanical strength. Comparing the values of the stress–intensity factor with those obtained in the tensile tests reported in Table 2, it could be inferred that the higher mechanical strength, the greater fracture toughness, and, consequently, the greater the energy required to propagate the crack.

The metallographic analysis of the areas adjacent to the fracture, illustrated in Fig. 7, reveals that cracks nucleate mainly around the notch and thereafter propagate through the graphite/matrix interface.

## Charpy impact test

Charpy impact test allows determining the toughness of a material, in terms of the absorbed energy because of the effect of dynamic loads. The results illustrated in Fig. 8 indicate that CG iron with ferritic matrix recorded the highest absorbed energy, reporting a value of 33·3 J. Pearlitic CG iron showed the lowest toughness, being its absorbed energy 14·3 J. The irons austempered at 300 and 350°C exhibited absorbed energy of 17·2 and 17·6 J respectively, while the austempered at 400°C recorded an absorbed energy of 28·4 J, close to the ferritic iron. The higher toughness with respect to the other austempered samples is because its greater retained austenite content, which confers major ductility.

Toughness exhibits the same tendency as ductility, reported in Table 2, indicating that the absorption energy capacity is greater as higher is the ductility.

The analysis of the fracture surface illustrated in Fig. 9 revealed that brittle cleavage mechanism is preponderant in all the samples, as a consequence of the small total plastic deformation that CG iron has. At the same time, decohesive rupture was observed, since the crack propagation occurs preferentially through the graphite/matrix interface, as shown in Fig. 7. Nevertheless, some areas with dimple rupture denoting ductile fracture were observed in the ferritic CG irons. In the pearlitic and in the austempered CG irons, it can be observed the facets corresponding to the transgranular fracture.

As mentioned previously, CG iron is suitable to manufacture mechanical components subjected to thermal shock or thermal fatigue. Under this operating condition, it is expected that the parts fissure, compromising its performance and integrity. In a previous work carried out in ADI,[26] it was assumed that the critical crack size is proportional to $(K_{IC}/\sigma_{yield})^2$, whereby $(K_{IC}/\sigma_{yield})$ is considered an adequate parameter to estimate the relative toughness of the materials. The critical crack size for each matrix is represented in Fig. 10, where it can be observed that the ferritic microstructure exhibits the highest value, as a consequence of its greater toughness and ductility reported in the Charpy and tensile tests. The matrices with lower toughness and ductility, as the pearlitic and the austempered at 300 and 350°C, showed a considerable decrease in the critical crack size. The ausferritic microstructure obtained at 400°C, instead, displayed a slight increase in this factor.

# Conclusions

Fracture toughness of CG iron with ferritic, pearlitic and ausferritic structures was evaluated to complement the available data concerning tensile and impact properties.

Ferritic matrix showed the lowest stress–intensity factor $K_{IC}$, indicating its lower resistance to crack propagation. $K_{IC}$ increases with normalising heat treatment; nevertheless, the higher values were recorded for the ausferritic structures, noting that $K_{IC}$ increases as the austempering temperature decreases. The results of the fracture toughness have shown a similar tendency to the mechanical strength; consequently, the higher UTS, the greater $K_{IC}$.

Another parameter of interest is the critical crack size, measured by $(K_{IC}/\sigma_{yield})^2$, from which it could be estimated the relative toughness of the material. CG iron with ferritic matrix recorded the greatest critical crack size with respect to the other samples. In the specific case of austempered CG irons, the higher critical crack size was obtained for the sample austempered at 400°C, since its greater content of retained austenite confers higher toughness and ductility.

The fracture surface corresponding to the different matrices was also analysed, observing that cleavage is the main mechanism of fracture. At the same time, decohesive rupture was observed in all samples, since the cracks propagate through the graphite/matrix interface.

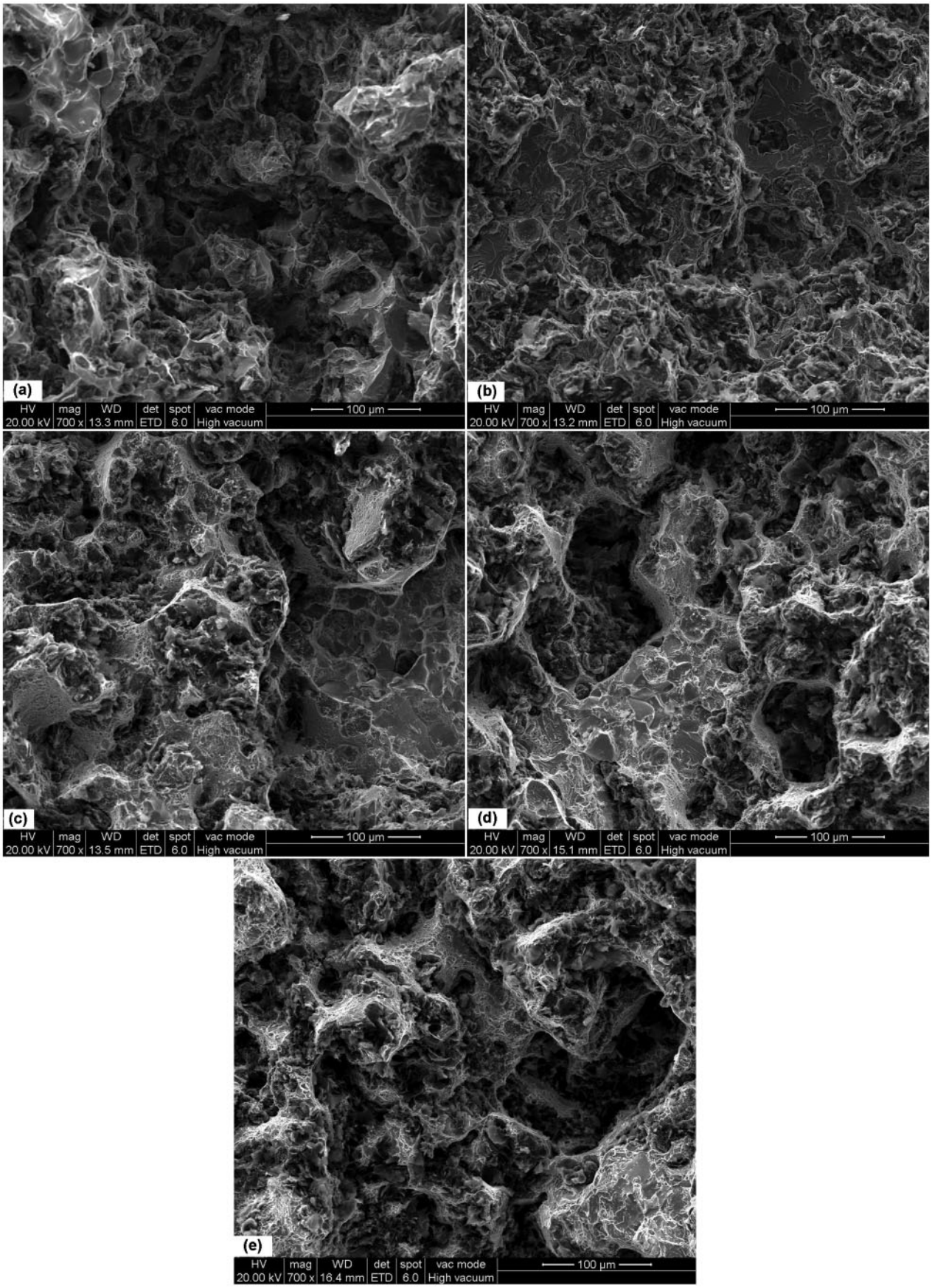


**9 Fracture surface corresponding to *a* ferritic, *b* pearlitic, *c* austempered at 300°C, *d* austempered at 350°C and *e* austempered at 400°C**

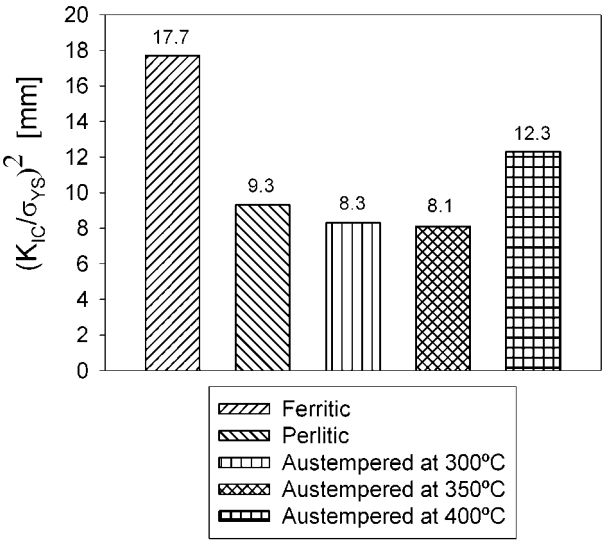


**10 Critical crack size factor**

## Acknowledgement

We thank the Comisión de Investigaciones Científicas de la Provincia de Buenos Aires (CICPBA) for the financial support to carry out the present research paper.

## References

1. I. Minkoff: 'The physical metallurgy of cast iron', Chap. 5, 'Solidification of spheroidal graphite cast iron', 102–133; 1983, Norwich, John Wiley & Sons.
2. A. Roviglione and J. D. Hermida: 'From flake to nodular: a new theory of morphological modification in gray cast iron', *Metall. Mater. Trans. B*, 2004, **35B**, 313–328.
3. I. Riposan, M. Chisamera, L. Sofroni and V. Brabie: 'Contributions to the study of the solidification mechanism and of the influence of structure on the properties of compacted/vermicular graphite cast iron', in 'The physical metallurgy of cast iron', (ed. H. Fredriksson and M. Hillert), Vol. 34, 131–140; 1985, New York, Elsevier Science Publishing Co. Inc.
4. D. M. Stefanescu: 'Solidification and modeling of cast iron—a short history of the defining moments', *Mater. Sci. Eng. A*, 2005, **A413–A414**, 322–333.
5. D. M. Stefanescu: 'Modeling of cast iron solidification – the defining moments', *Metall. Mater. Trans. A*, 2007, **38A**, 1433–1447.
6. G. L. Rivera, R. E. Boeri and J. A. Sikora: 'Solidification of gray cast iron', *Scr. Mater.*, 2004, **50**, 331–335.
7. R. E. Boeri and J. A. Sikora: 'Solidification macrostructure of spheroidal graphite cast iron', *Int. J. Cast Met. Res.*, 2001, **13**, 5, 307–313.
8. G. Rivera, R. Boeri and J. Sikora: 'Revealing and characterising solidification structure of ductile cast iron', *Mater. Sci. Technol.*, 2002, **18**, 691–697.
9. A. N. Roviglione and J. D. Hermida: 'A new unidirectional solidification method to study gray cast iron', *Metall. Mater. Trans. B*, 2002, **33B**, 235–241.
10. K. R. Ziegler and J. F. Wallace: 'The effect of matrix structure and alloying on the properties of compacted graphite iron', *AFS Trans.*, 1984, **92**, 735–748.
11. Y. J. Park, R. B. Gundlach, R. G. Thomas and J. F. Janowak: 'Thermal fatigue resistance of gray and compacted graphite cast iron', *AFS Trans.*, 1985, **93**, 415–422.
12. E. Nechtelberger, H. Puhr, J. B. von Nesselrode and A. Nakayasu: 'Cast iron with vermicular/compacted graphite – state of the art. Development, production, applications', Proc. 49th International Foundry Congress, Chicago, IL, USA, April 1982, CIATF, Paper 1, 1–39.
13. S. Dawson: 'Compacted graphite iron – a material solution for modern diesel engine cylinder blocks and heads', Proc. Conf. 68th World Foundry Cong., Chennai, India, February 2008, The Institute of Indian Foundrymen, 93–99.
14. W. L. Guesser, P. V. Duran and W. Krause: 'Compacted graphite iron for diesel engine cylinder blocks', Proc. Conf Congrès Le diesel: aujourd'hui et demain, May 2004, Lyon, France, Ecole centrale Lyon, 1–11.
15. Y. Wang, F. Hu, H. Shi and X. Fan: 'Application and development of vermicular iron to cylinder block castings' *Modern Cast Iron*, 2010, **06**, 23–26.
16. C.-H. Lim and B.-C. Goo: 'Development of compacted vermicular graphite cast iron for railway brake discs', *Met. Mater. Int.*, 2011, **17**, (2), 199–205.
17. A. X. Pan: 'Study on the casting defects of vermicular cast iron brake disc and the countermeasures', *Adv. Mater. Res.*, 2012, **472–475**, 2645–2649.
18. J. Desimoni, R. Gregorutti, K. Laneri, J. L. Sarutti and R. C. Mercader: 'Influence of the Mn content on the kinetics of austempering transformation in compacted graphite cast iron', *Metall. Mater. Trans. A*, 1999, **30A**, 2745.
19. K. F. Laneri, J. Desimoni, R. C. Mercader, R. W. Gregorutti and J. L. Sarutti: 'Thermal dependence of austempering transformation kinetics of compacted graphite cast iron', *Metall. Mater. Trans. A*, 2001, **32A**, 51–58.
20. R. Gregorutti, K. Laneri, J. Desimoni and R. C. Mercader: 'Study of the austempering transformation kinetics in compacted graphite cast irons', *Metall. Mater. Trans. A*, 2004, **35A**, 103–110.
21. H. Bayati, A. L. Rimmer and R. Elliott: 'The austempering kinetics and processing window in an austempered, low-manganese compacted-graphite cast iron', *Cast Met.*, 1994, **7**, (1), 11–24.
22. D. M. Stefanescu, R. Hummer and E. Nechtelberger: 'Compacted graphite irons', in 'ASM handbook', 9th edn, Vol. 15, 'Casting', (ed. J. R. Davis *et al.*), 667–677; 1988, Materials Park, OH, ASM International.
23. J. D. Landes: 'Fracture toughness testing', in 'ASM handbook', 9th edn, Vol. 8, 'Mechanical testing and evaluation', (ed. S. R. Lampman), 1302–1314; 2000, Materials Park, OH, ASM International.
24. A. Glover and G. Pollard: 'Deformation and fracture of gray cast iron structures', *J. Iron Steel Inst.*, 1971, 138–141.
25. T. Venkatasubramanian and T. Baker: 'Fracture toughness of flake graphite cast iron', *Met. Technol.*, 1978, **5**, 57–61.
26. R. A. Martínez, R. E. Boeri and J. A. Sikora: 'Impact and fracture properties of ADI, compared with SAE 4140 steel', *AFS Trans.*, 1998, **106**, 27–30.